DIFFERENTIAL CROSS-SECTION OF $\Sigma^+(1189)$ IN PHOTO-PRODUCTION

CHANDRA S. NEPALI AND MOSKOV AMARYAN
Old Dominion University
and
The CLAS Collaboration

Analysis note (version 1) submitted to the CLAS Collaboration for a review.
July 11, 2012

CONTENTS

ABSTRACT

Differential cross-section of $\Sigma^+(1189)$ production has been measured in photo-production on a hydrogen target by using *g11a* data set in the photon energy range 1.6-3.5 GeV. The Σ^+ is produced in the reaction $\gamma p \rightarrow \Sigma^+ K^0$ with subsequent decay to proton and π^0. Here K^0 is a mixture of CP eigenstates K_S and K_L. In this experiment only decay products π^+ and π^- of short lived K_S are detected. So, detected final state particles are proton, π^+ and π^-. The π^0 is reconstructed from the missing mass of all detected charged particles, and K_s is reconstructed in the invariant mass of $\pi^+\pi^-$. The Σ^+ is reconstructed from its decay products proton and π^0. Our results are in good agreement with previous CLAS and SAPHIR results.

List of Figures

Chapter 1

Introduction

One of the main goals of the hadronic physics is to study the structure of the nucleon, its excited states, and to understand the underlying mechanism of their production. Experimentally, most of the baryon resonances are discovered in pion elastic scattering experiments. These excited states consist of many states, each of them with a large width up to a few hundred MeV. Interpretation of the experimental data and the extraction of parameters of resonances is extremely difficult because of the overlap and interference of these states with each other. Also, because of the large coupling constant at low energy perturbative QCD is not applicable in resonance region. The constituent quark model based predictions are able to explain the mass spectrum of the experimentally observed resonances quit well but they also predict other resonances which have not been observed experimentally yet. Based on the quark model, the number of excited states is determined by the effective degrees of freedom. The reasons for not observing those resonances may either be explained by an uncertainty in the number of degrees of freedom used by the models or by assuming that the unobserved resonances do not couple strongly to the $N\pi$ channels in which most of the resonances have been observed.

Models like quark-pair creation [1] or collective string-like three quark models [2] showed substantial decay branches of baryon resonances into $K\Lambda$ and $K\Sigma$ channels. So, kaon production experiments are important tools to study baryon resonances.

Hyperon cross section in photo-production has been measured by many experiments like SAPHIR [3], CB-ELSA/TAPS [4, 5, 6], CLAS [7, 8, 9] and LEPS [10]. For Σ^+ production these data are limited to 2.4 GeV photon energy. All these results agree well, however CB-ELSA/TAPS shows cusp like structure in the region between $K^*\Lambda$ and $K^*\Sigma^+$ thresholds which is not visible in other measurements.

CHAPTER 2

DATA ANALYSIS

2.1 INTRODUCTION

We have used g11a data set with Bremsstrahlung tagged photon beam [11] on a liquid hydrogen target. The experiment was carried out at electron energy 4.01860 GeV for run numbers 43490 - 44107 and 5.02114 GeV for run numbers 44108 - 44133 [12]. Photon beam is produced by Bremsstrahlung of an electron in a thin radiator. The photon energy ranges from 0.8 GeV to 4.8 GeV for whole range of electron energy. The average electron current for the runs used in this analysis is about 63 nA. The target cell is 40 cm long, placed 10 cm upstream of the CLAS center.

In this analysis, we are using Σ^+ (1189), produced via process, Fig. 2.1,

$$\gamma + p \rightarrow K^0 + \Sigma^+(1189)$$

where K^0 is a mixture of K_s and K_L [13, 14, 15, 16], which are eigenstates of CP.

$$|K^0 >= \frac{1}{\sqrt{2}}(|K_S > + |K_L >)$$

Then, K_S, being short lived meson, decays quickly to π^+ and π^- with branching ratio 69% via CP conserving weak decay while K_L, being long lived meson, decays beyond the detector, making it undetectable. Σ^+ decays to proton and π^0 with branching ratio 51% via CP conserving weak decay. So, final detected particles are proton, π^+, and π^-. Σ^+ and K_S are reconstructed from their decay products.

$$\begin{aligned}\gamma + P &\rightarrow K_s + \Sigma^+ \\ &\rightarrow \pi^+ + \pi^- + p + \pi^0\end{aligned}$$

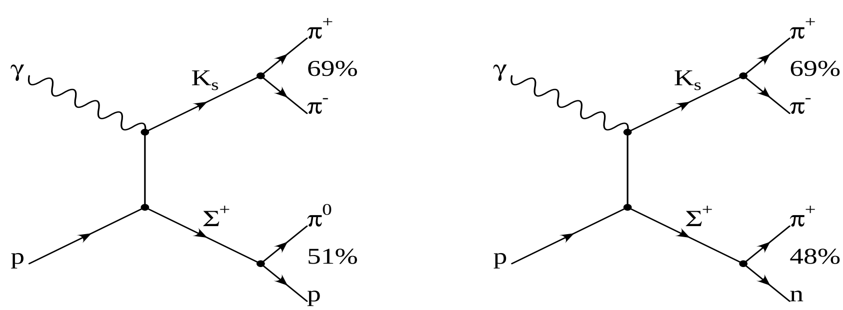

(a) $\Sigma^+ \rightarrow p + \pi^0$ decay (b) $\Sigma^+ \rightarrow n + \pi^+$ decay

Fig. 2.1: Photo-production of Σ^+.

2.2 Event selection

Inclusive events with 1 detected proton, 1 detected π^+ and 1 detected π^- are selected from EVNT bank. Photon, with status 7 or 15 (flag for good electrons with successful tagger reconstruction) [17], whose tag-time is in coincidence with start-time is selected under the condition that there is no other photon within ±2ns, [18] in order to make sure that we are selecting right photon [1]. The photon distribution are shown in Fig: 2.2. K_s is reconstructed from invariant mass of π^+ and π^-, π^0 is reconstructed from missing mass of proton, π^+, and π^-, and Σ^+ is reconstructed from missing mass of π^+ and π^-.

$$M(\pi^+\pi^-) \Rightarrow K_s; \quad MM(P\pi^+\pi^-) \Rightarrow \pi^0; \quad MM(\pi^+\pi^-) \Rightarrow \Sigma^+$$

Tagger correction is applied to the photon energy using CLAS g11 tagger correction package [19]. Energy loss

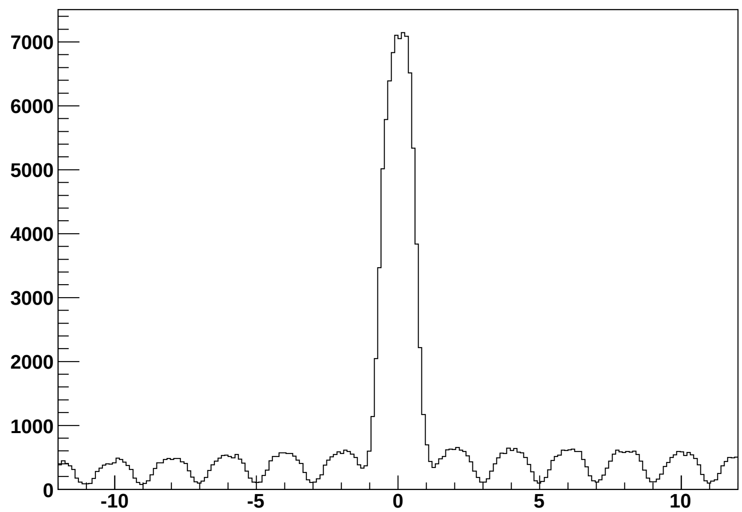

Fig. 2.2: Figure shows the (tag time-start time) distribution for photons with status 7 or 15 written in the TAGR bank of the BOS file.

correction and momentum correction are applied to all detected charged particles by using the CLAS energy loss package (eloss) [20], and CLAS g11 momentum correction package [19]. The tagger correction factor is shown in Fig: 2.3 and total missing mass distributions before and after all corrections (tagger + eloss + momentum corrections) are shown in Fig: 2.4, which clearly shows the effect of these corrections.

2.3 Sources of background

- direct production of final particles:

$$\gamma + P \rightarrow P + \pi^+ + \pi^- + \pi^0$$

[1] For photon selection: first we selected one photon whose tag time is closest to the start time, and then we checked the condition 'is there any other photon within ±2ns window of this selected photon?'. If there was another photon within ±2ns window then that event was removed. This make sure that we are selecting only one photon. ±2ns cut is tighter cut than ±1ns cut. We have checked ±2ns vs ±1ns and we found that the difference is less than 1% with all other cuts (cuts used in this anlaysis) applied and less than 3% without any cut. We did not select the photon by just taking the cut ±2ns around 0, because this may include more than 1 photon if above mentioned condition is not imposed

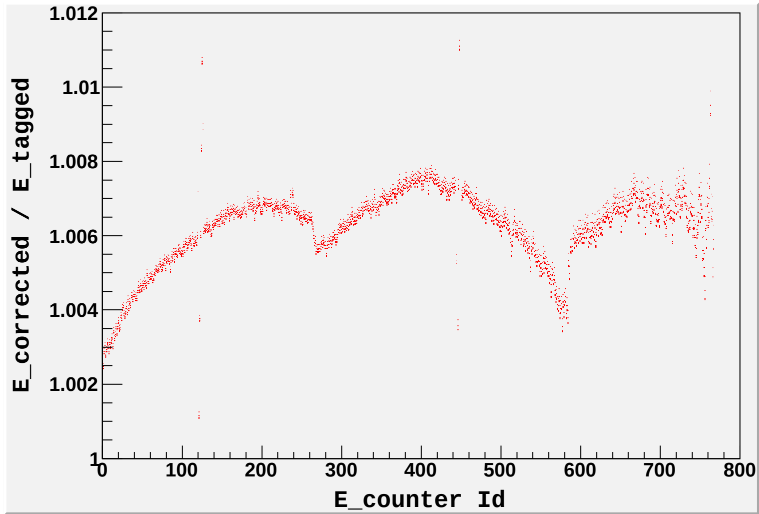

Fig. 2.3: Photon energy correction factor vs E-counter Id.

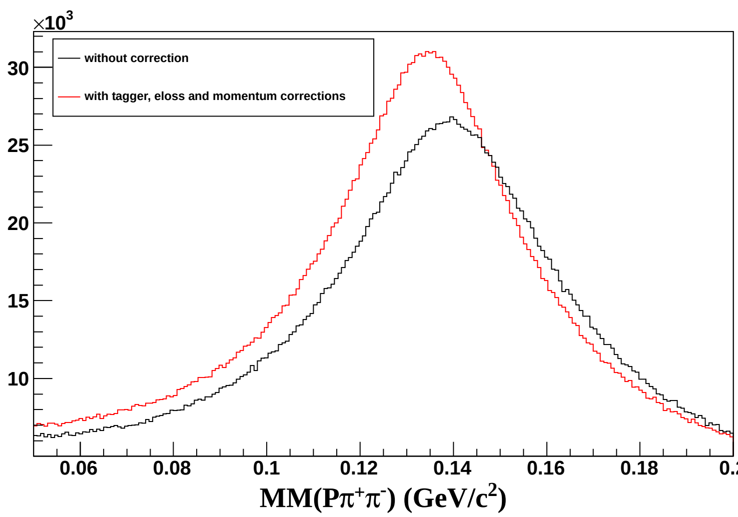

Fig. 2.4: Missing mass distribution of proton and two opposite charged pions, before and after all corrections (taggre + eloss + momentum corrections). After the corrections, the peak center is very close to the π^0 mass of 135 MeV.

- due to production of ω via

$$\gamma + P \rightarrow P + \omega \rightarrow P + \pi^+ + \pi^- + \pi^0$$

- due to miss-identification of protons as kaons.
- due to miss-identification of kaons as pion. However, invariant mass of two charged pions as K_S will be larger than mass of K_S and those events will be removed by mass cut on K_S. So, this does not contribute in the background.

Fig: 2.5(a) shows the missing mass distribution of the proton without any cut. It clearly shows $\eta(547)$, $\eta^{'}(958)$, $\omega(782)$, $\phi(1020)$, and $f_1(1285)$ mesons produced with proton. Fig: 2.5(b) shows the missing mass distribution of the proton under Σ^+ (peak of $p\pi^0$ mass spectrum). It clearly shows the $\omega(782)$ under Σ^+, contributing to the background in Σ^+ distribution. Fig. 2.5(c) shows that the overlap of the tail of the photon in $MM(p\pi^+\pi^-)$ with the π^0 in $MM(p\pi^+\pi^-)$ is negligible. Fig. 2.5(d) shows that the contribution form the miss-identified kaons as protons (red line) is negligible. Combining these figures show that the background under the Σ^+ is mostly due to ω production, and direct production of proton and pions.

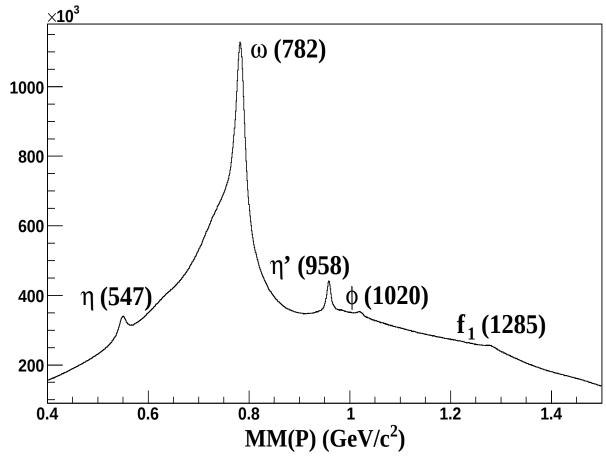

(a) Missing mass of proton

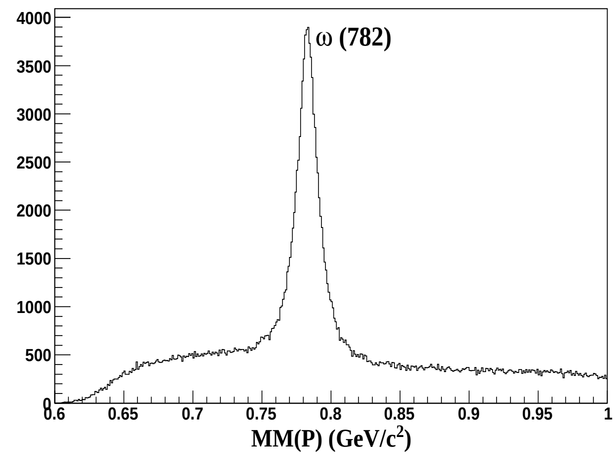

(b) Missing mass of proton under Σ^+

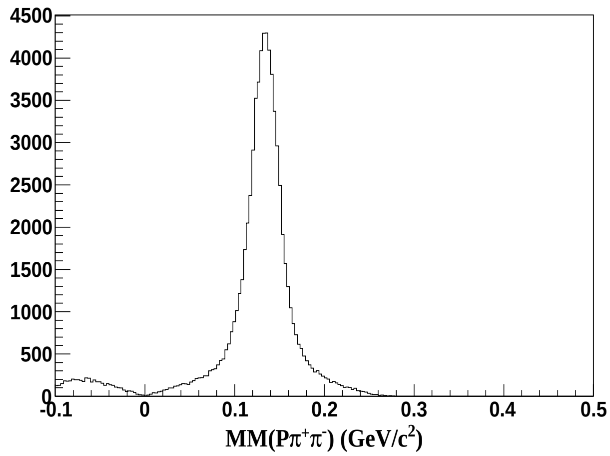

(c) Missing mass of proton, π^+ and π^- under Σ^+

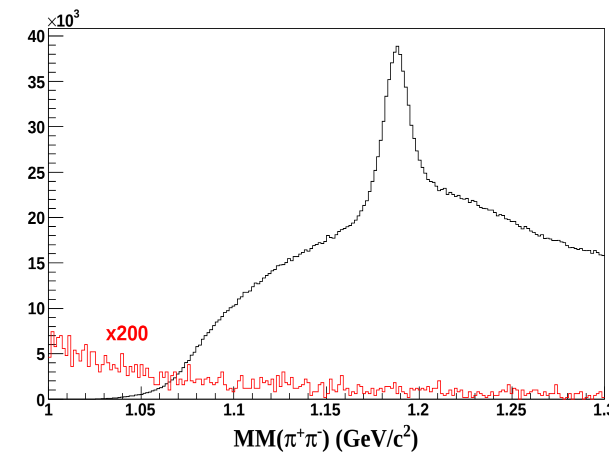

(d) Missing mass of π^+ and π^- with a kaon is miss-identified as a proton

Fig. 2.5: (a) Missing mass of proton without any cut, showing η, η', ω, ϕ, and f_1 mesons. (b) Missing mass of proton with $|MM(p\pi^+\pi^-) - 0.135| < 0.02$, $|M(\pi^+\pi^-) - 0.4976| < 0.02$, $|MM(\pi^+\pi^-) - 1.189| < 0.02$ cuts. (c) Missing mass of proton, π^+ and π^- under Σ^+. (c) shows that the overlap of the photon tail with π^0 is negligible. (d) red line (scaled up by a factor 200) shows the $MM(\pi^+\pi^-)$ distribution where mass of the kaon is used for identified proton. As we can see that the contribution to background from miss-identified kaon as proton is negligible. These figures clearly shows that background under the Σ^+ is mostly due to ω production, and direct production of proton and pions.

2.4 KINEMATIC CUTS

In order to select Σ^+ from the reaction and decay mode under consideration, and also to minimize the background we have used few kinematic cuts. The effect of these cuts on particle reconstruction will be shown below. The cuts used are:

1. cut on invariant mass of two charged pions to select K_s, $|M(\pi^+\pi^-) - 0.497| < 3\sigma$ GeV/c^2.

2. cut on missing mass of proton and two charged pions to select π^0, $|MM(p\pi^+\pi^-) - 0.135| < 3\sigma$ GeV/c^2.

Fig. 2.6(a) shows the missing mass of proton, π^+ and π^-; Fig. 2.6(b) shows the mass of two charged pions with π^0 selected in $MM(p\pi^+\pi^-)$; Fig. 2.6(c) shows the missing mass of two charged pions with π^0 selected in $MM(p\pi^+\pi^-)$ and K_S selected in $M(\pi^+\pi^-)$. Blue lines are fit to the peak (gaussian function) and background (polynomial function).

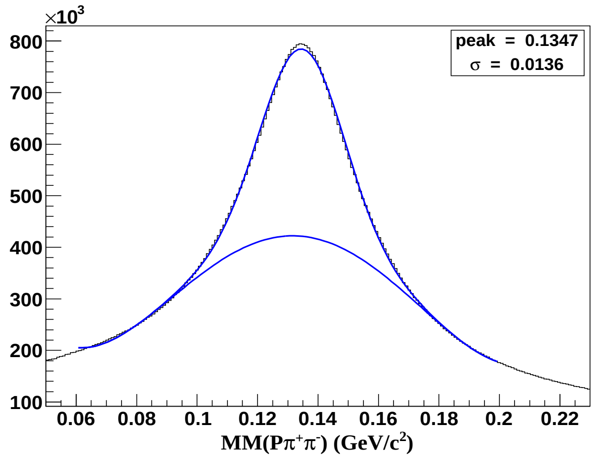

(a) missing mass of proton, π^+, and π^-

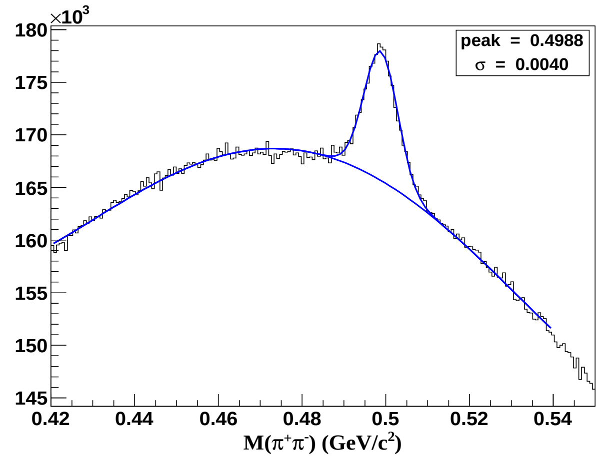

(b) mass of π^+, and π^-

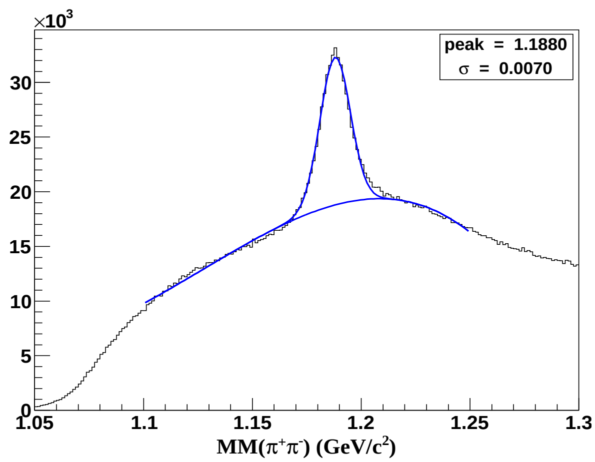

(c) missing mass of π^+, and π^-

Fig. 2.6: (a) Missing mass of proton, π^+, and π^- without any cut, (b) mass of π^+ and π^- with π^0 selected in $MM(P\pi^+\pi^-)$, (c) missing mass of π^+ and π^- with π^0 selected in $MM(P\pi^+\pi^-)$ and K_S selected in $M(\pi^+\pi^-)$.

2.5 BACKGROUND SUBTRACTION

Fig. 2.7 shows the $MM(\pi^+\pi^-)$ distribution where $\pm 3\sigma$ is selected around K_S peak in mass of $\pi^+\pi^-$ for the black line, and 3σ from left and right in side-band of K_S is selected for the red line. As we can see that the side band of the K_s reproduces the background perfectly. So, we used side band of the K_s as a background to do background subtraction. Figs. 2.8 and 2.9 show the distributions of the $MM(\pi^+\pi^-)$ after background subtraction.

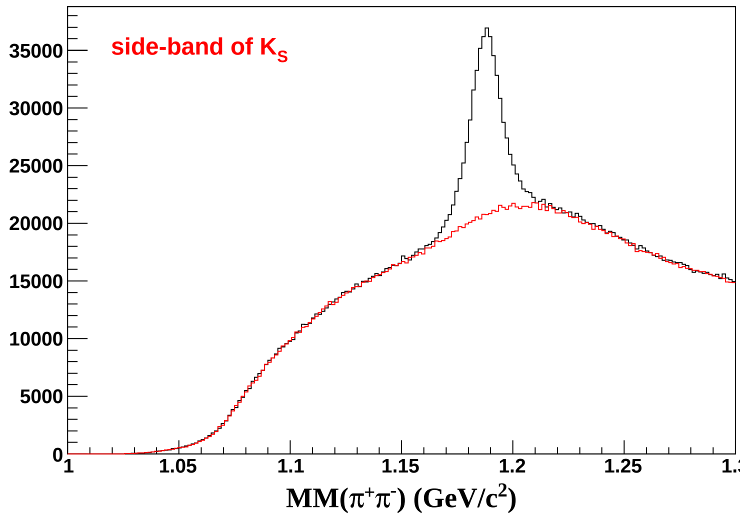

Fig. 2.7: MM($\pi^+\pi^-$) distribution with background from side-band of K_S.

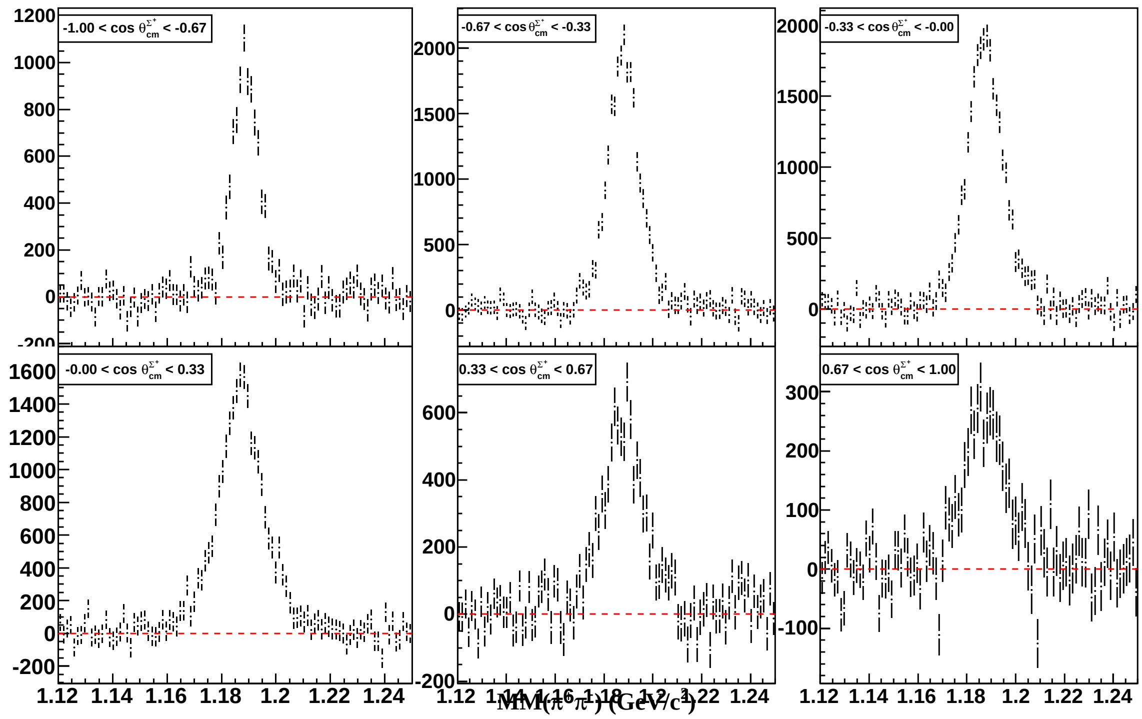

Fig. 2.8: MM($\pi^+\pi^-$) distribution after background subtraction.

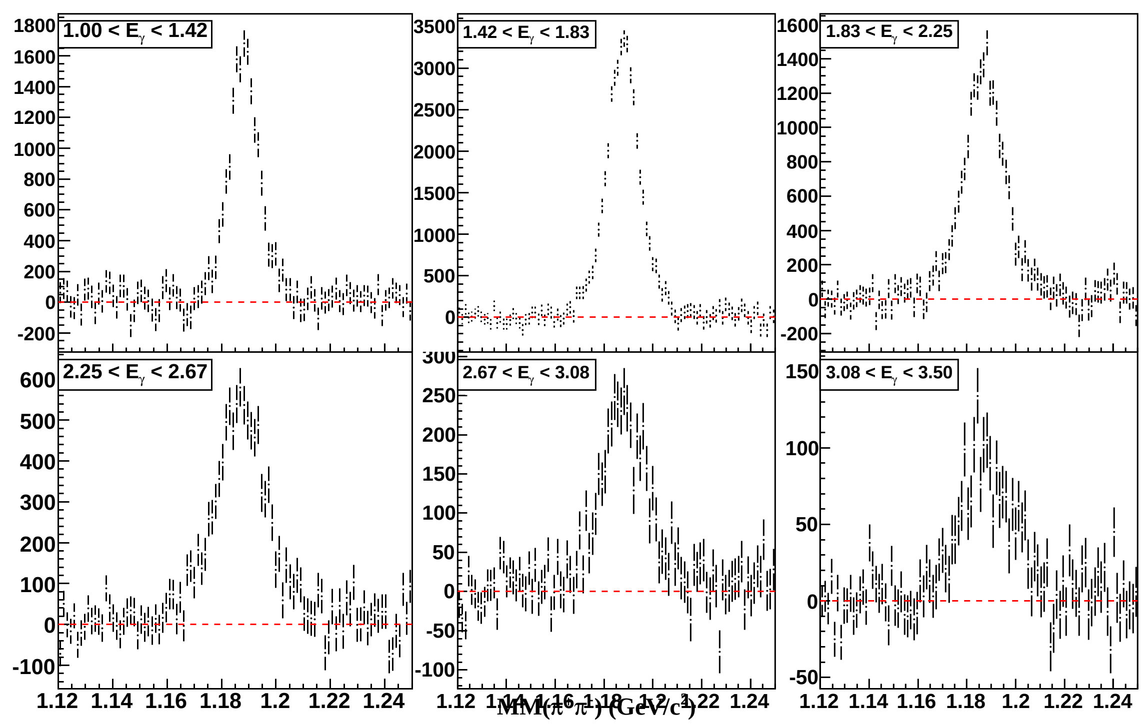

Fig. 2.9: MM($\pi^+\pi^-$) distribution before background subtraction.

CHAPTER 3

SIMULATION: ACCEPTANCE CORRECTION

Monte Carlo events are generated based only on kinematics [21], and uniform angular distributions of Σ^+'s decay products (for detail about the simulation please see the analysis note [22]). The generated events are passed through gsim and gpp, the ffread card and gpp flags are shown in Appendix: 7.1. The output from gpp is passed through recsis with tcl file shown in Appendix: 7.1.

$$\boxed{\text{Event Generator}} \Longrightarrow \boxed{\text{GSIM}} \Longrightarrow \boxed{\text{GPP}} \Longrightarrow \boxed{\text{RECSIS}}$$

Figs. 3.1 show ϕ vs θ acceptance region of the CLAS for proton and pions. The gaps show the gaps between drift-chamber sectors. For comparison purposes, accepted region from the data is also shown in Fig.:3.2.

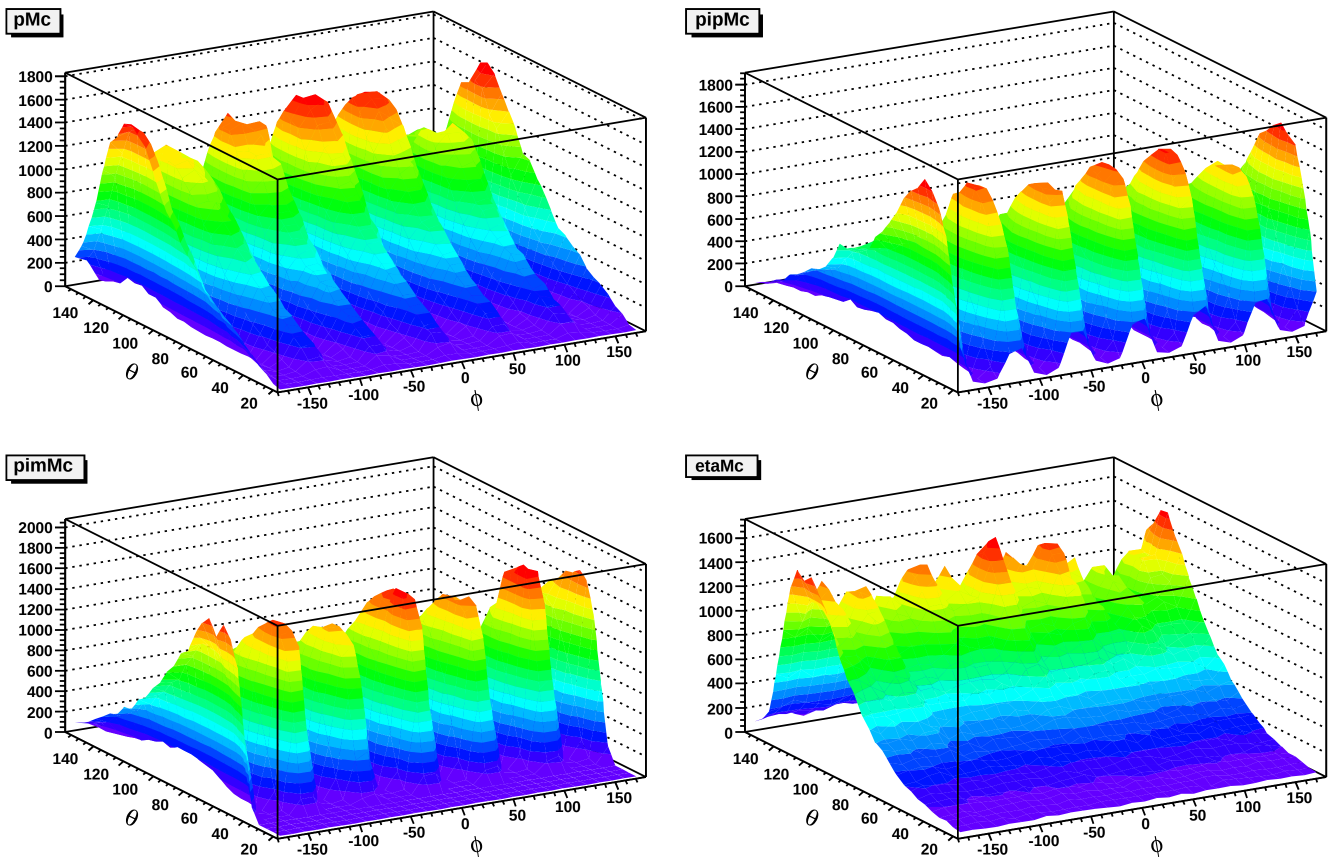

Fig. 3.1: Acceptance region from MC simulation, $\phi \sim \theta$, for proton (top left), π^+ (top right), and π^- (bottom), integrated over all other variables.

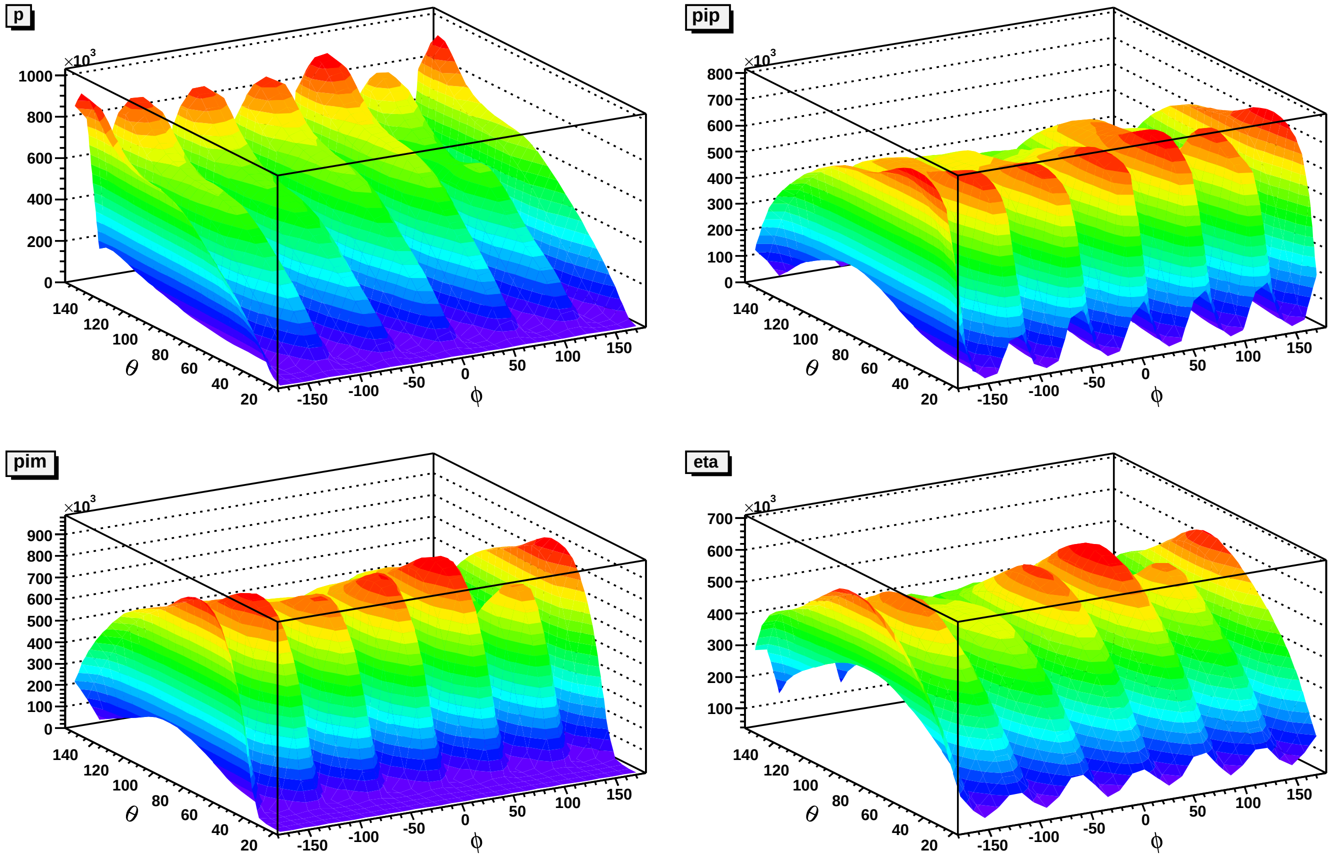

Fig. 3.2: Acceptance region from data, $\phi \sim \theta$, for proton (top left), π^+ (top right), and π^- (bottom), integrated over all other variables.

3.1 Kinematic fit

We saw that (see Fig.: 3.4) the mass of the reconstructed particles, $MM(\pi^+\pi^-)$, is shifted by about 3 MeV from the pdg value. So, we did kinematic fit of the simulated data by using the CLAS kinematic fit package. We did 1C kinematic fit (with π^0 as missing particle). Kinematic fitting brought the mass of the reconstructed particle close to the pdg value. Fig. 3.3 shows confidence level of the kinematic fit. The pull distributions and confidence level show that the fit is reasonable. A cut of greater than 10% in confidence level is applied. The mass of the reconstructed particles, as shown in Fig. 3.4, are at the right places. MC events must cover all the kinematic ranges as in the real data. Fig. 3.5 shows the t_{Σ^+} distribution from the real data (red line) and from the accepted MC events (black line). Similarly, Fig. 3.6 show the momentum, polar angle and azimuthal angle of all the detected particles as well as reconstructed Σ^+ along with the photon energy. Black lines are from the real data and red lines are from accepted MC events. As we can see, MC events cover full range of kinematic variables as in the real data.

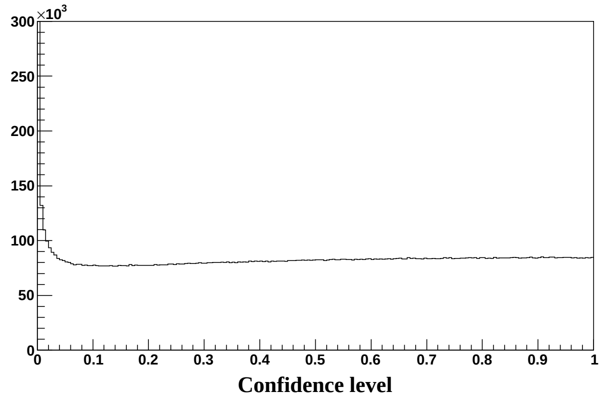

Fig. 3.3: Confidence level of the kinematic fit.

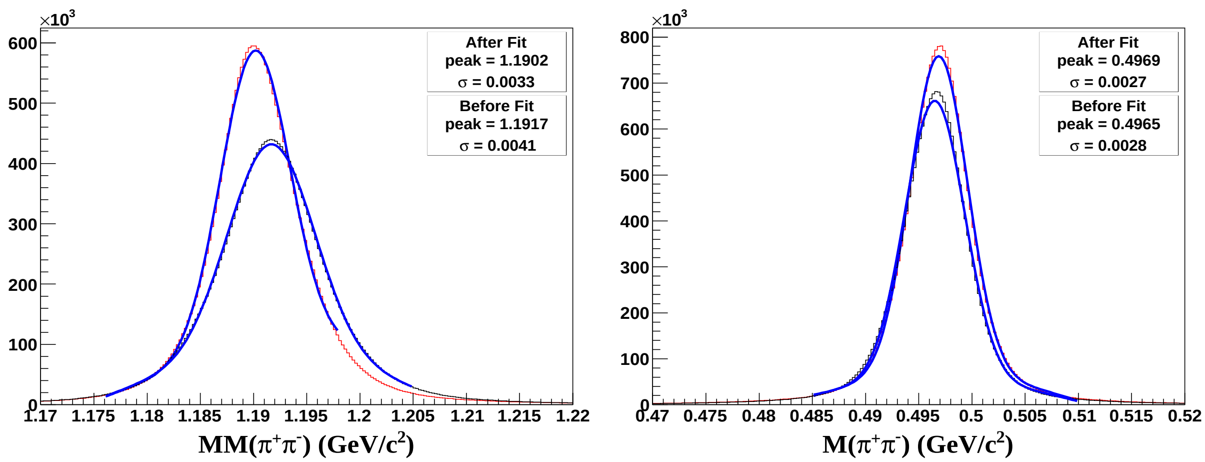

Fig. 3.4: Mass of reconstructed Σ^+ and K_s. Red lines show distribution with kinetic fit and black lines show distribution without kinetic fit. Blue lines are gaussian fit to the distribution with kinetic fit.

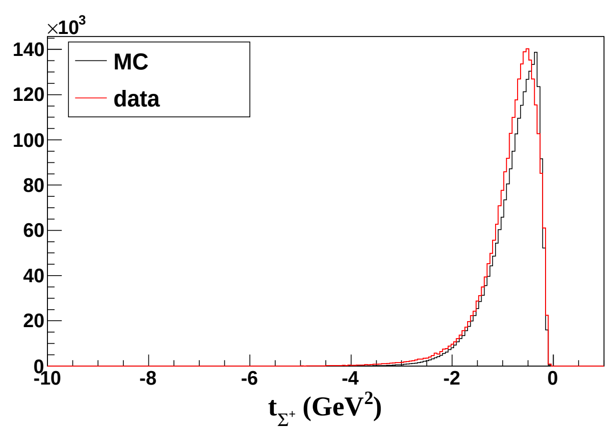

Fig. 3.5: t-distribution from the real data (red line) and accepted MC events (black line).

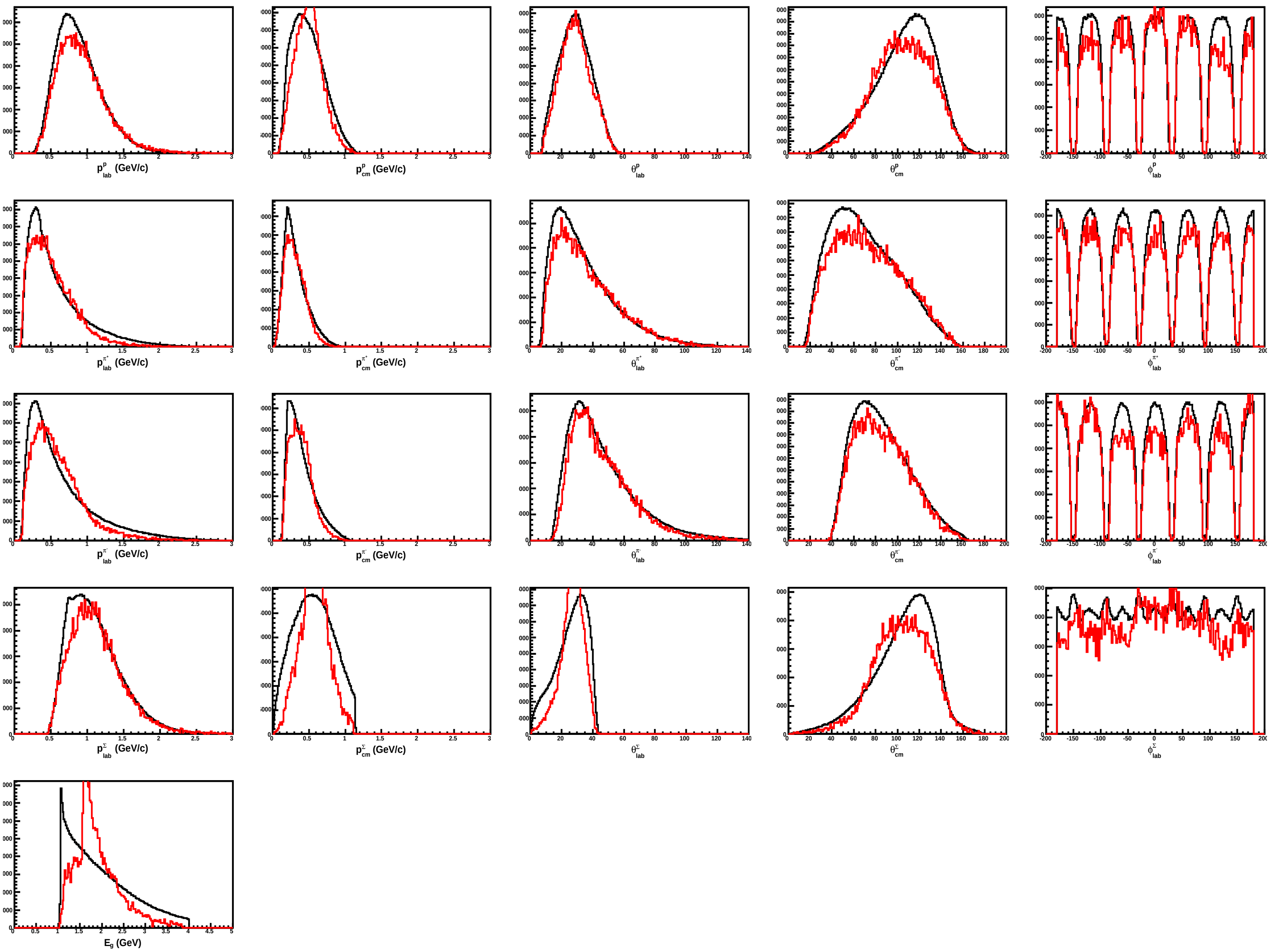

Fig. 3.6: Figures show different kinematic coverage range from MC and real data. First row is for proton, second row if for π^+, third row is for π^-, fourth row is for Σ^+ and fifth row is for photon energy. Similarly, First column is for momentum in lab frame, second column is for momentum in cm frame, third column is for θ in lab frame, fourth column is for θ in cm frame and fifth column is for azimuthal angle ϕ.

3.2 Acceptance correction

Σ^+ from accepted MC events (MC events accepted after passing though GSIM and GPP) are selected by same procedure as in real data by applying $\pm 3\sigma$ cut around the peak. The acceptance function for each kinematic bin is calculated by dividing accepted events by generated events in that kinematic bin. Then, data is corrected by dividing it with acceptance function for that kinematic bin. The acceptance function is

$$A[E_\gamma, \cos(\theta_{K_s})_{cm}] = \frac{N_{\mathrm{a}}[E_\gamma, \cos(\theta_{K_s})_{cm}]}{N_{\mathrm{g}}[E_\gamma, \cos(\theta_{K_s})_{cm}]} \tag{3.1}$$

where N_{g} and N_{a} are the number of generated and accepted events. Fig. 3.7 and Fig. 3.8 show the acceptance vs photon energy and acceptance vs $\cos(\theta_{K_s})_{cm}$ respectively.

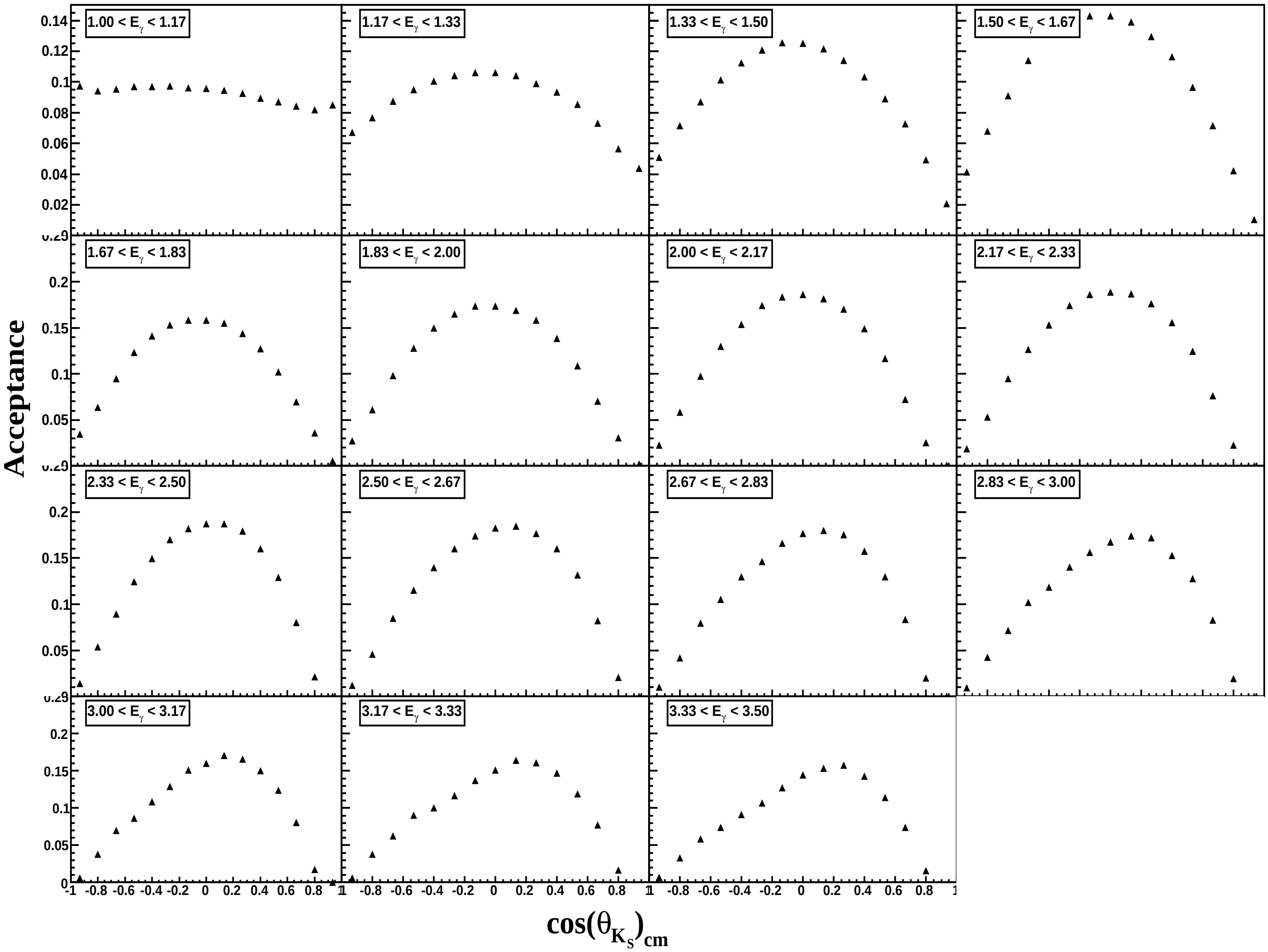

Fig. 3.7: Acceptance vs $\cos(\theta_{K_s})_{cm}$ for different photon energy bins.

3.3 Acceptance error

Since the acceptance function is obtained by dividing the accepted events by the generated events, the error in the acceptance function is calculated by

$$\triangle A(E_\gamma, \cos\theta_{cm}) = A(E_\gamma, \cos\theta_{cm}) \sqrt{\left(\frac{\triangle N_{\text{a}}(E_\gamma, \cos\theta_{cm})}{N_{\text{a}}(E_\gamma, \cos\theta_{cm})}\right)^2 + \left(\frac{\triangle N_{\text{g}}(E_\gamma, \cos\theta_{cm})}{N_{\text{g}}(E_\gamma, \cos\theta_{cm})}\right)^2} \tag{3.2}$$

where $\triangle N_{\text{a}}(E_\gamma, \cos\theta_{cm}) = \sqrt{N_{\text{a}}(E_\gamma, \cos\theta_{cm})}$ and $\triangle N_{\text{g}}(E_\gamma, \cos\theta_{cm}) = \sqrt{N_{\text{g}}(E_\gamma, \cos\theta_{cm})}$.

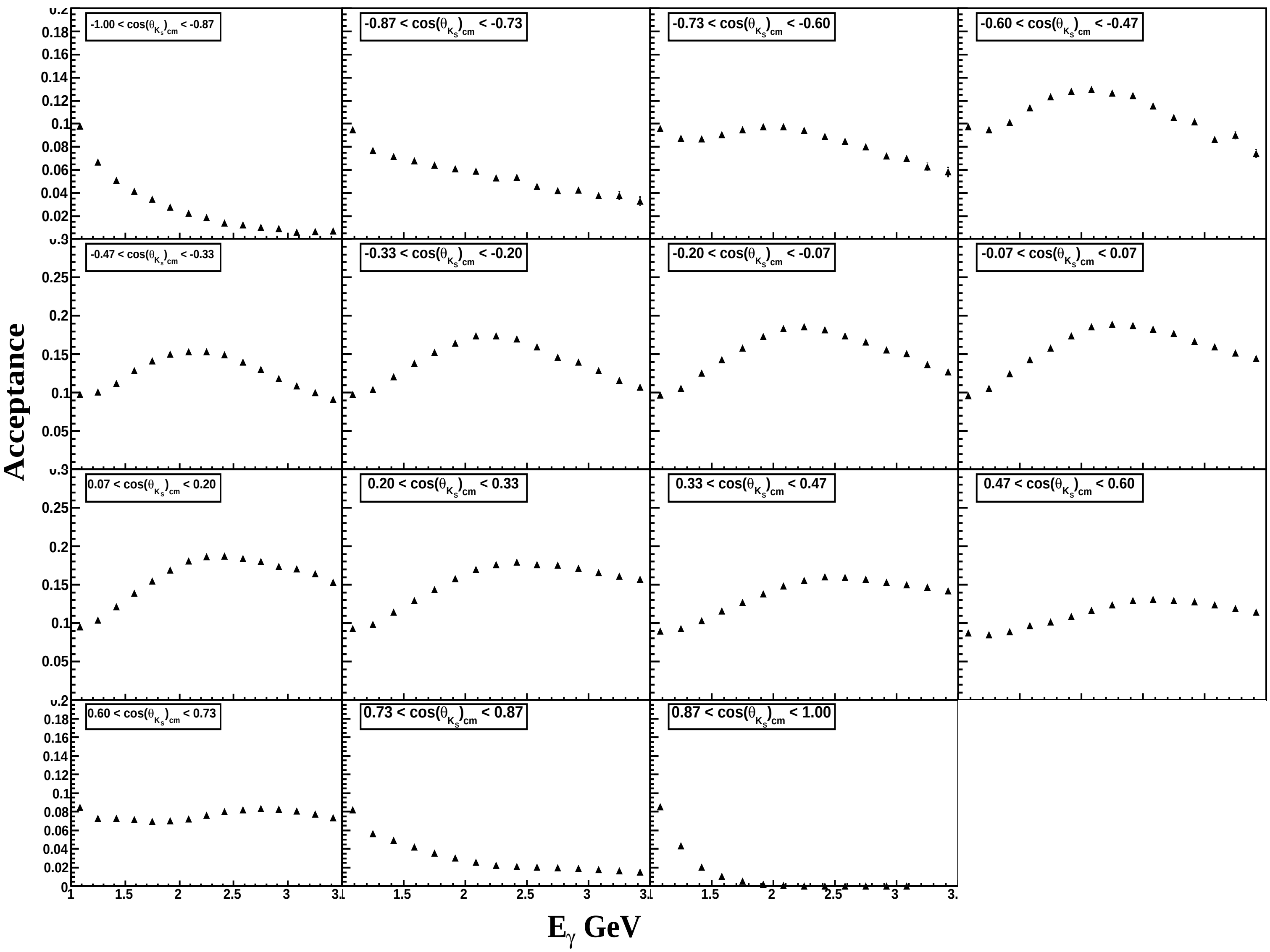

Fig. 3.8: Acceptance vs photon energy for different $\cos(\theta_{K_s})_{cm}$ bins.

CHAPTER 4

CALCULATION PROCEDURE

4.1 TARGET PROPERTIES

The g11a target was liquid hydrogen with cell length 40 cm. In order to calculate the production probability, the number of target protons available to the photon beam are required. The density changes due to change in temperature and pressure during the different runs. The temperature and pressure are measured and stored in CLAS database for each run. The average density calculated based on the parameterization [23]

$$\rho = a\, T^2 + b\, P + c \tag{4.1}$$

is

$$\overline{\rho} = 0.07177 \;\; \text{g/cm}^3 \tag{4.2}$$

And the variance is

$$\sigma^2_{flux} = \frac{1}{N_{run} - 1} \sum_{run} (\rho_{run} - \overline{\rho})^2 \tag{4.3}$$

$$= 6.776 \times 10^{-9} \;\; \text{g}^2/\text{cm}^6 \tag{4.4}$$

where ρ_{run} is the density in each run. The variance is about 0.11%.

4.2 PHOTON FLUX

Photon flux is calculated by using CLAS *gflux* [17] package.

First, total yield (Y_r) for each run is calculated whose statistical error is $\triangle Y_r = \sqrt{N}$ and is shown in Fig. 4.1(a). Then total flux (F_r) for each run is added and the flux normalized total yield for each run

$$N_r = \frac{Y_r}{F_r} \tag{4.5}$$

is calculated. The error for this flux normalized total yield is given by

$$\triangle N_r = N_r \sqrt{\left(\frac{\triangle Y_r}{Y_r}\right)^2 + \left(\frac{\triangle F_r}{F_r}\right)^2} \tag{4.6}$$

Fig. 4.1(b) shows the run-by-run flux normalized yield which is nearly flat as expected.

4.3 PHOTON ENERGY VS PHOTON FLUX

Photon flux and error from *gflux* is obtained for each E-counter run-by-run. These are combined together to get flux vs photon energy. Flux errors are combined in quadrature. Fig. 4.2 shows the total flux vs photon energy.

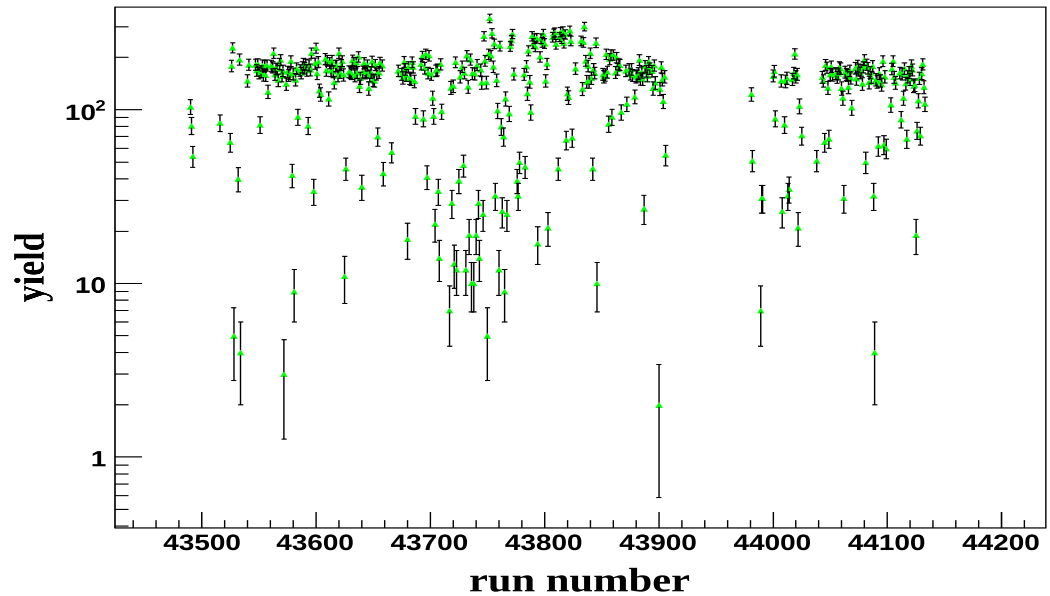

(a) run by run total yield

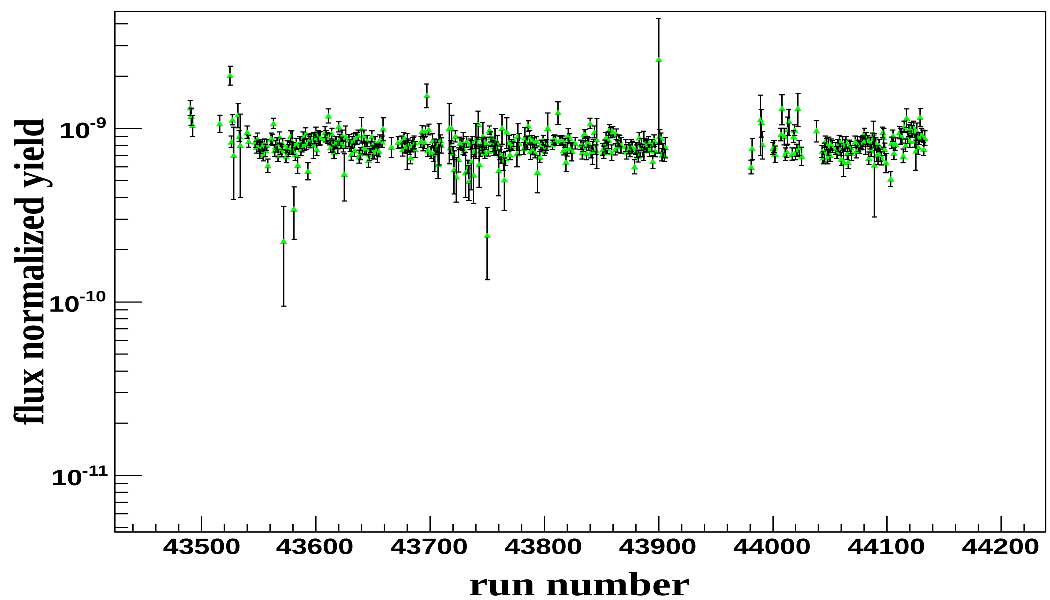

(b) run by run flux normalized total yield

Fig. 4.1: Run by run total yield and flux normalized total yield.

4.4 CROSS SECTION

The differential cross-section of Σ^+ production is given by

$$\frac{d\sigma(E_\gamma, \cos\theta_{cm})}{d\cos\theta_{cm}} = \frac{Y(E_\gamma, \cos\theta_{cm})}{F(E_\gamma)\ T\ A(E_\gamma, \cos\theta_{cm})\ \delta\cos\theta_{cm}\ B} \tag{4.7}$$

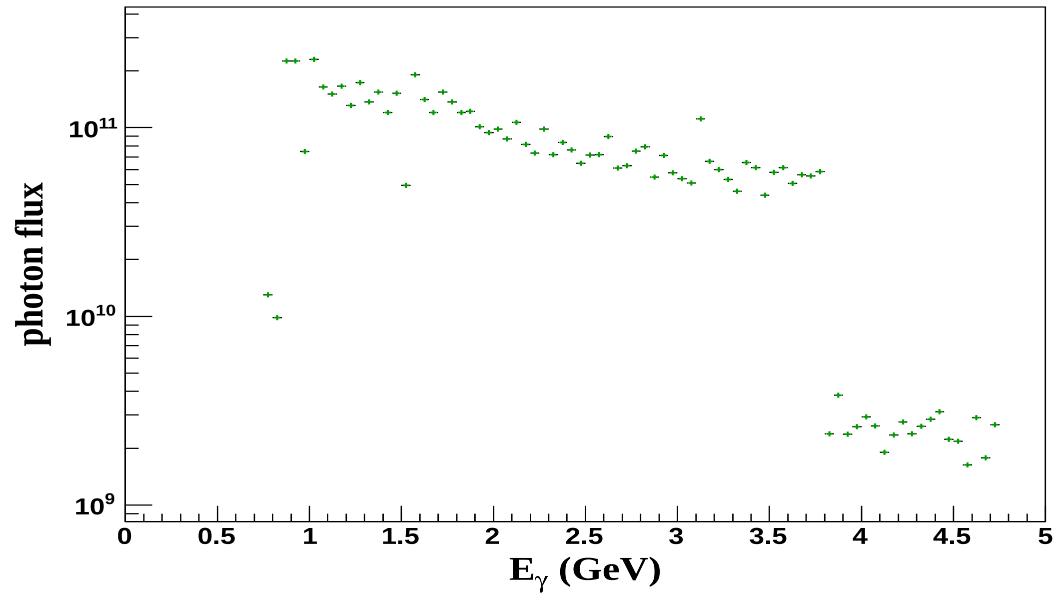

Fig. 4.2: Photon energy vs total photon flux

where

$$Y(E_\gamma, \cos\theta_{cm}) \rightarrow \Sigma^+ \text{ yield} \tag{4.8}$$

$$F(E_\gamma) \rightarrow \text{photon flux} \tag{4.9}$$

$$T \rightarrow \text{ number of target proton per unit area} \tag{4.10}$$

$$A(E_\gamma, \cos\theta_{cm}) \rightarrow \text{detection acceptance} \tag{4.11}$$

$$B \rightarrow \text{product of branching ratios of } K_S \text{ and } \Sigma^+ \tag{4.12}$$

$$\delta\cos\theta_{cm} \rightarrow \text{size of } \cos\theta_{cm} \text{ bin} \tag{4.13}$$

The number of the target proton per unit area is given by

$$T = \frac{N_A\,\rho\,L}{N} \tag{4.14}$$

where N_A is Avogadro's number, ρ is the target density, L is the target length and N is the number of grams per mole of the target. Then,

$$\boxed{\frac{d\sigma(E_\gamma, \cos\theta_{cm})}{d\cos\theta_{cm}} = \frac{Y(E_\gamma, \cos\theta_{cm})}{F(E_\gamma)\;A(E_\gamma, \cos\theta_{cm})\;\delta\cos\theta_{cm}\;B}\;\frac{N}{N_A\,\rho\,L}} \tag{4.15}$$

Similarly,

$$\boxed{\frac{d\sigma(E_\gamma, \cos\theta_{cm})}{dE_\gamma} = \frac{Y(E_\gamma, \cos\theta_{cm})}{F(E_\gamma)\;A(E_\gamma, \cos\theta_{cm})\;\delta E_\gamma\;B}\;\frac{N}{N_A\,\rho\,L}} \tag{4.16}$$

B, product of branching ratios for $\Sigma^+ \rightarrow p + \pi^0$ and $K_S \rightarrow \pi^+ + \pi^-$ = 0.5 × 0.5157 × 0.6920 = 0.1784322.

CHAPTER 5

RESULTS

Differential cross section vs $\cos\theta_{K_s}$ and E_γ are shown in Figs. 5.1 and 5.2 respectively. Errors are statistical only.

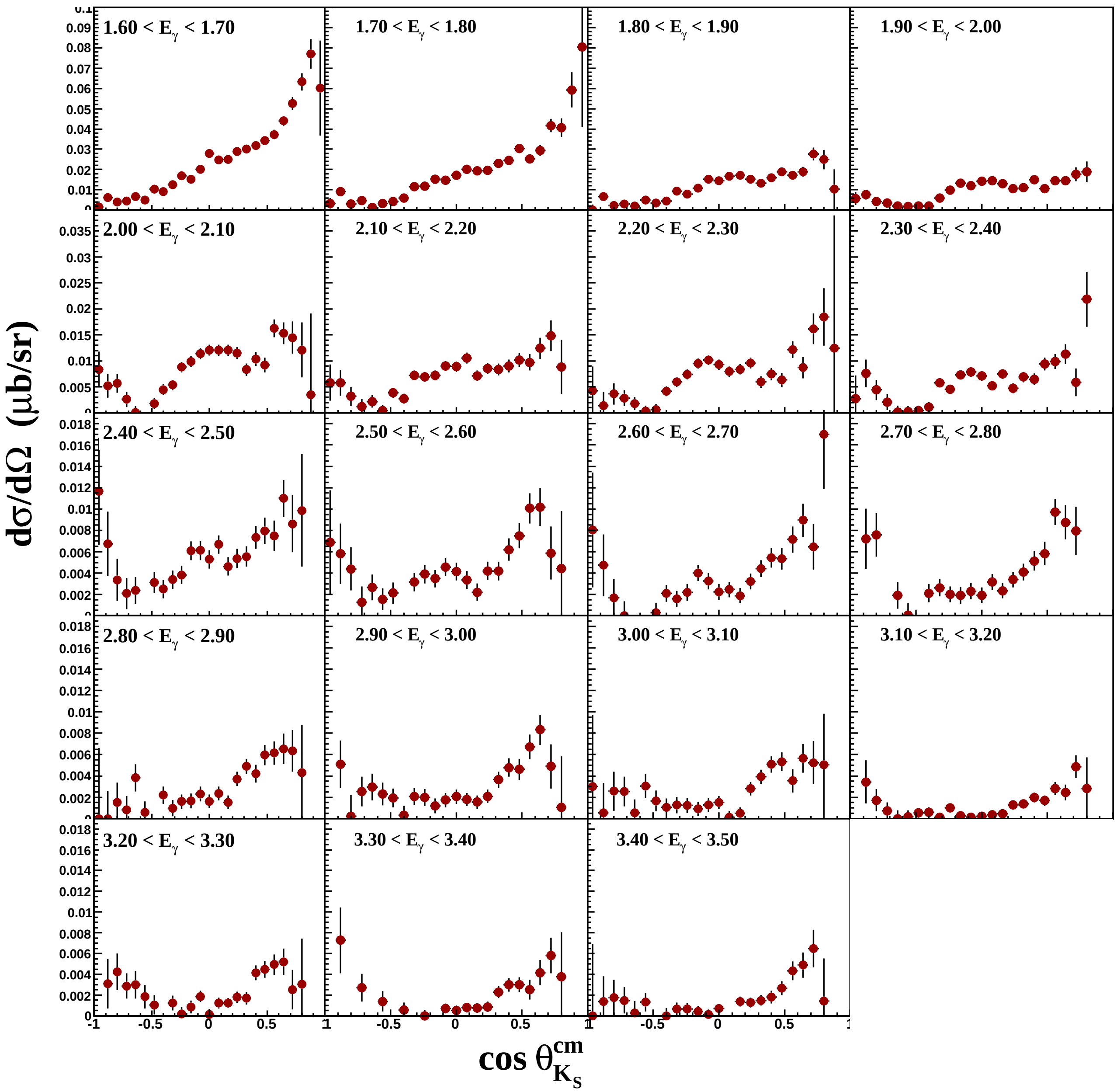

Fig. 5.1: $d\sigma/d\Omega$ vs $\cos\theta_{K_s}$ for different photon energy bins. Errors are statistical only.

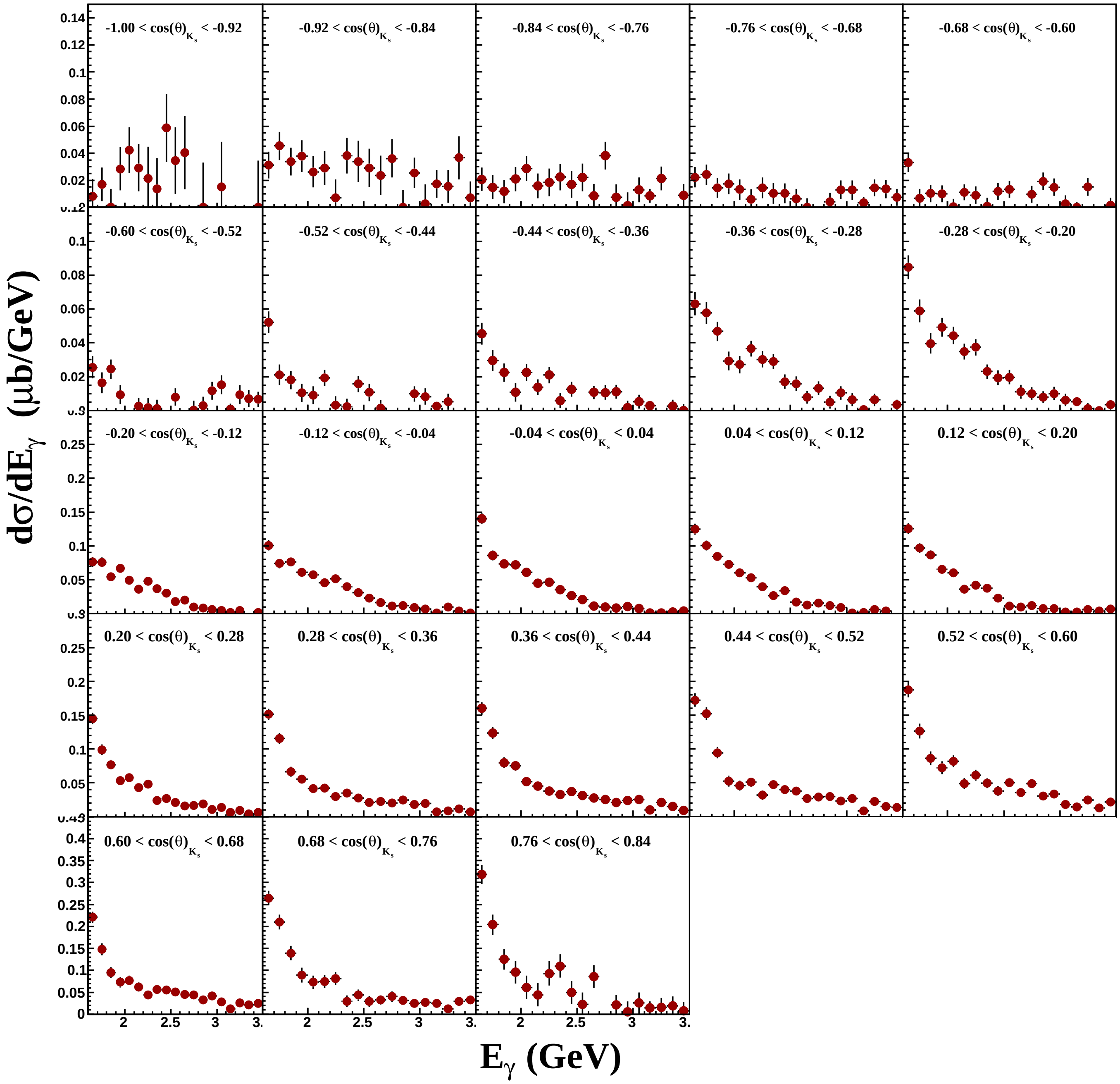

Fig. 5.2: $d\sigma/dE_\gamma$ vs E_γ for different $\cos\theta_{K_s}$ bins. Errors are statistical only.

CHAPTER 6

DISCUSSION AND SUMMARY

We have compared our results with SAPHIR [24] and CLAS [25], and are shown Figs. 6.1 and 6.2 respectively. The functional behavior of the cross section from our result is in very good agreement with others, however there is a small difference in magnitude.

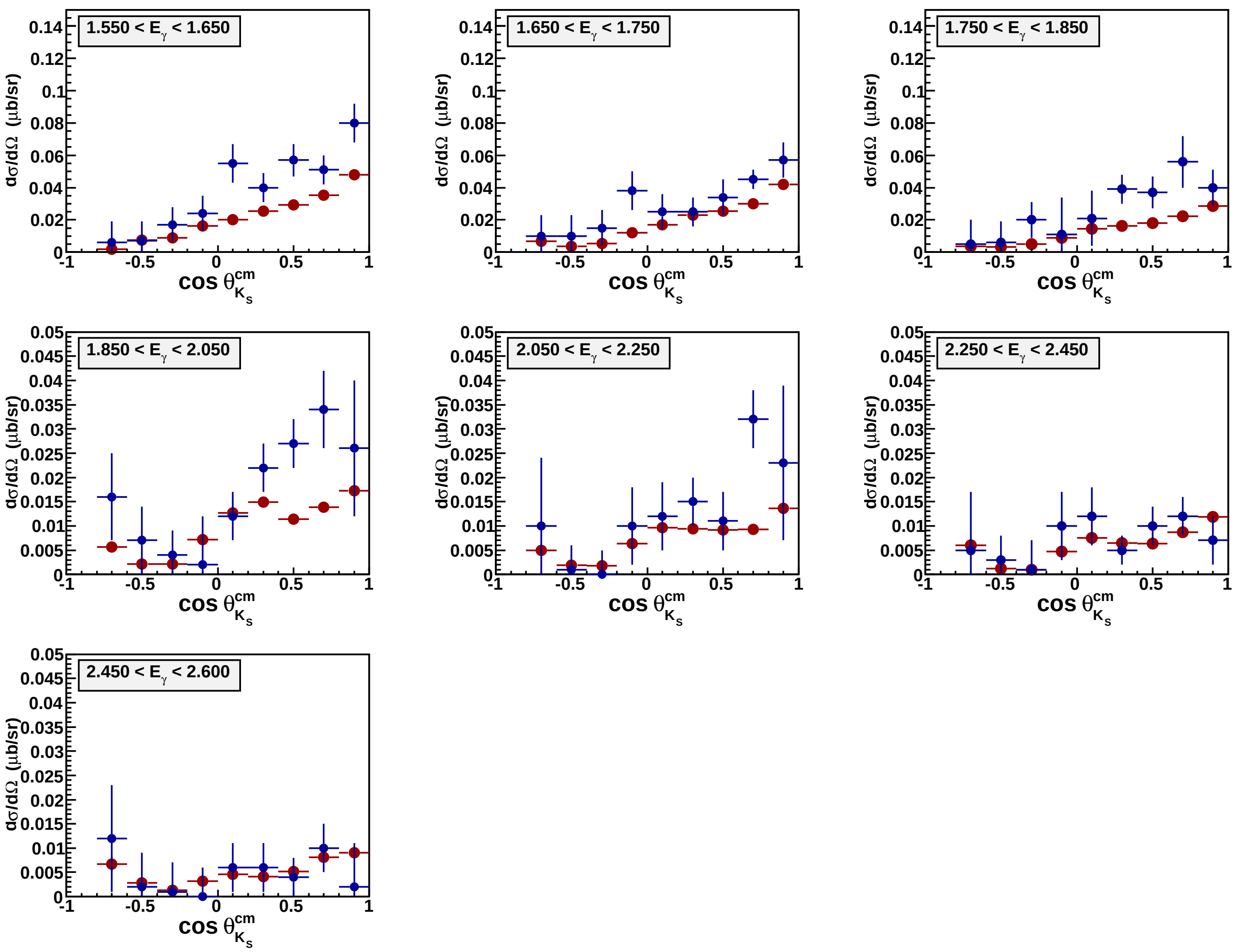

Fig. 6.1: Comparison plots with SAPHIR result. Red makers are our results and blue markers are SAPHIR results **??**.

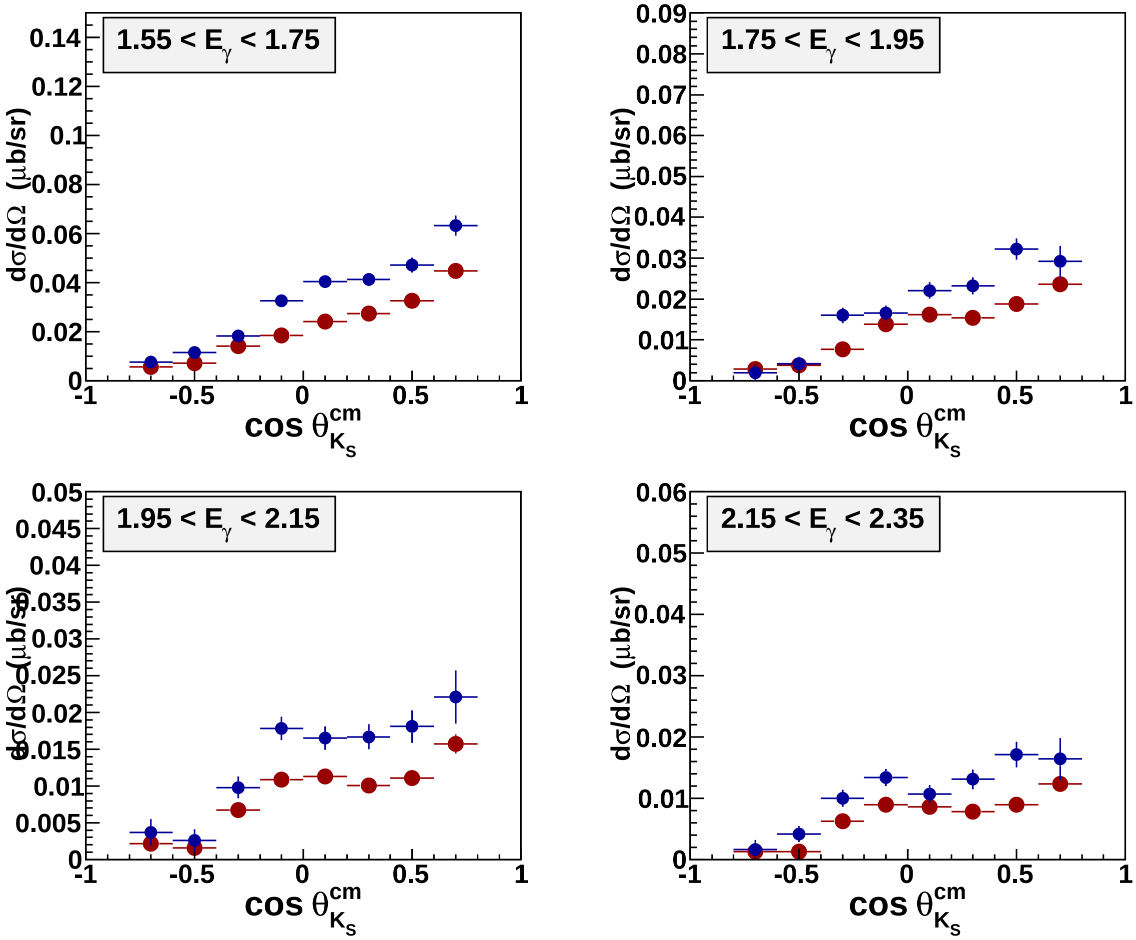

Fig. 6.2: Comparison plots with previous CLAS result. Red makers are our results and blue markers are previous CLAS results **??**.

Chapter 7

Appendix

7.1 Appendix I

7.1.1 ffread card for gsim

```
LIST
KINE 1
AUTO 1
MAGTYPE 2
MAGSCALE 0.4974 0.0
FIELD 2
STTYPE 1
STZOFF -10.0
TGPOS 0.0 0.0 0.0
TARGET 'g11a'
TGMATE 'PROT'
GEOM 'ALL'
NOGEOM 'EC1' 'CC' 'MINI' 'PTG'
NOSEC OTHE
BEAM 4.018
CUTS 5.e-3 5.e-3 5.e-3 5.e-3 5.e-3
DCCUTS 1.e-4 1.e-4 1.e-4 1.e-4 1.e-4
ECCUTS 1.e-4 1.e-4 1.e-4 1.e-4 1.e-4
SCCUTS 1.e-4 1.e-4 1.e-4 1.e-4 1.e-4
STCUTS 5.e-5 5.e-5 5.e-5 5.e-5 5.e-5
NSTEPMAX 20000
TIME 1000000 1000000 1000000
RUNG 43832
TRIG 1000000
RNDM 128 128
STOP
```

7.1.2 gpp flags

```
gpp -P0x1f -ooutputFile -a2.0 -b1.8 -c1.8 -f0.8 -Y -R44100 inputFile
```

7.1.3 tcl file for recsis

```
source /u/group/clas/builds/PRODUCTION/packages/tcl/recsis_proc.tcl;
turnoff ALL;
global_section off;
turnon seb trk tof egn user pid;
inputfile InputFile;
setc chist_filename histfile;
setc log_file_name logfile;
setc outbanknames(1) ”all”;
outputfile outfile PROC 2047;
setc prlink_file_name ”prlink_g11_1920.bos”;
setc bfield_file_name ”bgrid_T67to33.fpk”;
set torus_current 1920;
set mini_torus_current 0;
set poltarget_current 0;
set TargetPos(3) -10.;
set trk_maxiter 8;
set trk_minhits(1) 2;
set trk_lrambfit_chi2 50.;
set trk_tbtfit_chi2 70.;
set trk_prfit_chi2 70.;
set trk_statistics 3 ;
set dc_xvst_choice 0;
set def_adc -1;
set def_tdc -1;
set def_atten -1;
set def_geom -1;
set st_tagger_match 15.;
set lst_do -1;
set lpid_make_trks 0;
set photon_trig_type 4;
fpack ”timestop -9999999999”
setc rec_prompt ”CLASCHEF_recsis> ”;
go 2000000;
exit_pend;
```

BIBLIOGRAPHY

[1] S. Capstick and W. Roberts, Phys. Rev. D **58**, 074011 (1998) [nucl-th/9804070].

[2] R. Bijker, F. Iachello and A. Leviatan, Phys. Rev. D **55**, 2862 (1997) [nucl-th/9608057].

[3] K. H. Glander, J. Barth, W. Braun, J. Hannappel, N. Jopen, F. Klein, E. Klempt and R. Lawall *e*t al., Eur. Phys. J. A **19**, 251 (2004) [nucl-ex/0308025].

[4] R. Castelijns *et al.* [CBELSA/TAPS Collaboration], Eur. Phys. J. A **35**, 39 (2008) [nucl-ex/0702033 [NUCL-EX]].

[5] M. Nanova *et al.* [CBELSA/TAPS Collaboration], Eur. Phys. J. A **35**, 333 (2008) [arXiv:0803.2146 [nucl-ex]].

[6] H. Schmieden, J. Phys. Conf. Ser. **349**, 012006 (2012).

[7] R. Bradford *et al.* [CLAS Collaboration], Phys. Rev. C **73**, 035202 (2006) [nucl-ex/0509033].

[8] M. E. McCracken *et al.* [CLAS Collaboration], Phys. Rev. C **81**, 025201 (2010) [arXiv:0912.4274 [nucl-ex]].

[9] S. A. Pereira *et al.* [CLAS Collaboration], Phys. Lett. B **688**, 289 (2010) [arXiv:0912.4833 [nucl-ex]].

[10] M. Sumihama *et al.* [LEPS Collaboration], Phys. Rev. C **73**, 035214 (2006) [hep-ex/0512053].

[11] D. I. Sober, H. Crannell, A. Longhi, S. K. Matthews, J. T. O'Brien, B. L. Berman, W. J. Briscoe, P. L. Cole *et al.*, Nucl. Instrum. Meth. **A440**, 263-284 (2000).

[12] M. Ungaro, R. De Vita, L. Elouadrhiri, g11 data processing, CLAS-NOTE 2005-14.

[13] M. Gell-Mann and A. Pais, Phys. Rev. **97**, 1387 (1955).

[14] A. Pais, O. Piccioni, Phys. Rev. **100**, 1487-1489 (1955).

[15] H. Georgi, *Weak Interactions and Modern Particle Theory*, Benjamin/cummingas, Menlo Park, USA (1984) 165p.

[16] E. D. Commins, P. H. Bucksbaum, *Weak Interactions Of Leptons And Quarks*, Cambridge University Press, Cambridge, USA (1983) 473p.

[17] J. Ball, E. Pasyuk, *Photon Flux Determination Through Sampling of "out-of-time" Hits with the Hall B Photon Tagger*, CLAS-NOTE:2005-002.

[18] M. Battaglieri and R. De Vita, *Study of the ω photoproduction differential cross section at 90 deg from g11 and test of quark counting rules*, CLAS approved analysis.

[19] CLAS package /u/group/clas/builds/release-f8-2/packages/utilities/g11pcor

[20] CLAS package /u/group/clas/builds/release-f8-2/packages/eloss

[21] W-M Yao *et al.* (Particle Data Group), J. Phys. G: Nucl. Part. Phys. **33** 1 (2006).

[22] Chandra Nepali and Moskov Amaryan, Transverse Polarization of $\Sigma^+(1189)$ in Photo-production on a Hydrogen Target, CLAS approved analysis.

[23] R. Bradford and R. A. Schumacher, *Liquid Hydrogen Density in the G1C CLAS Cryostat*, CLAS Note 2002-003.

[24] R. Lawall, J. Barth, C. Bennhold, K. -H. Glander, S. Goers, J. Hannappel, N. Joepen and F. Klein *e*t al., Eur. Phys. J. A **24**, 275 (2005) [nucl-ex/0504014].

[25] B. Carnahan, Ph. D. Thesis, Catholic University of America, Washington, USA (2003) [CLAS Collaboration], F. J. Klein [CLAS Collaboration], Nucl. Phys. A **754**, 321 (2005).